electronics

MDPI

Article

Design of the New Dual-Polarized Broadband Phased Array Feed Antenna for the Sardinia Radio Telescope

Paolo Maxia [1,*], Giovanni Andrea Casula [2,*], Alessandro Navarrini [3], Tonino Pisanu [4], Giuseppe Valente [5], Giacomo Muntoni [2] and Giorgio Montisci [2]

[1] Italian National Institute for Astrophysics (INAF), Astronomical Observatory of Cagliari (OAC), 09047 Selargius, Italy
[2] Department of Electrical and Electronic Engineering (DIEE), University of Cagliari, 09123 Cagliari, Italy; giacomo.muntoni@unica.it (G.M.); giorgio.montisci@unica.it (G.M.)
[3] NRAO (National Radio Astronomy Observatory), Charlottesville, VA 22903, USA; alessandro.navarrini@inaf.it
[4] Institute for Space Astrophysics and Planetology (IAPS), Italian National Institute for Astrophysics (INAF), 00133 Rome, Italy; tonino.pisanu@inaf.it
[5] Italian Space Agency (ASI), 00133 Rome, Italy; giuseppe.valente@asi.it
* Correspondence: paolo.maxia@inaf.it (P.M.); andrea.casula@unica.it (G.A.C.)

Abstract: High-sensitivity and large-scale surveys are essential in advancing radio astronomy, enabling detailed exploration of the universe. A Phased Array Feed (PAF) installed in the focal plane of a radio telescope significantly enhances mapping efficiency by increasing the instantaneous Field of View (FoV) and improving sky sampling capabilities. This paper presents the design and optimization of a novel C-Band Phased Array Feed antenna for the Sardinia Radio Telescope (SRT). The system features an 8×8 array of dual-polarized elements optimized to achieve a uniform beam pattern and an edge taper of approximately 5 dB for single radiating elements within the 3.0–7.7 GHz frequency range. The proposed antenna addresses key efficiency limitations identified in the PHAROS 2 (PHased Arrays for Reflector Observing Systems) system, including the under-illumination of the Sardinia Radio Telescope's primary mirror caused by narrow sub-array radiation patterns. By expanding the operational bandwidth and refining the radiation characteristics, this new design enables significantly improved performance across the broader frequency range of 3.0–7.7 GHz, enhancing the telescope's capability for wide-field, high-resolution observations.

Keywords: phased array feeds; broadband antennas; Sardinia Radio Telescope

Academic Editors: Manuel Arrebola and Paolo Baccarelli

Received: 24 December 2024
Revised: 11 February 2025
Accepted: 17 February 2025
Published: 19 February 2025

Citation: Maxia, P.; Casula, G.A.; Navarrini, A.; Pisanu, T.; Valente, G.; Muntoni, G.; Montisci, G. Design of the New Dual-Polarized Broadband Phased Array Feed Antenna for the Sardinia Radio Telescope. *Electronics* **2025**, *14*, 807. https://doi.org/10.3390/electronics14040807

1. Introduction

High sensitivity and survey speed are crucial for radio astronomical applications, enabling studies of galactic gas, magnetic fields, and cosmological surveys. These factors depend on the number of radiated beams, the solid angle each beam covers, the bandwidth, and the system temperature. To enhance these capabilities and increase the Field of View (FoV), multiple sky regions can be observed simultaneously by using a multi-feed horn system or a Phased Array Feed (PAF).

A Phased Array Feed (PAF) installed at a radio telescope's focal plane enhances survey speed and sky sampling capacity compared to traditional multi-feed horn systems [1–4]. It consists of a planar array of small antenna elements arranged in a regular two-dimensional grid, with inter-element spacing of about half a wavelength at the highest frequency. This design optimizes sky coverage and prevents grating lobes [5–7].

In a Phased Array Feed, multiple beams are electronically synthesized by combining signals from subsets of antenna elements, called "sub-arrays", using an analog or digital beamforming network controlled by specialized software. Each element contributes to multiple beams, which can be fine-tuned across a wide frequency range by adjusting the phase and amplitude of the signals [8].

The performance of a Phased Array Feed depends not only on its overall array configuration but also on the radiation patterns of the individual antenna elements. Different antenna layouts, such as patch antennas and folded dipoles, have been explored for this purpose. Among these, Vivaldi antennas are frequently used due to their broad operating bandwidth, low cross-polarization levels, and wide radiated beams [9]. The size and geometry of individual antenna elements influence the beam shape: consequently, the radiation pattern of each individual antenna plays a crucial role in the array overall performance. By carefully combining the amplitudes and phases of the elements of the Phased Array Feed it is possible to synthesize beams with the desired shape and characteristics.

The main component of a radio astronomy receiver is a large parabolic dish that collects and focuses incoming radio waves onto the feed antenna. A key design goal is to maximize the G/T_{sys} ratio, where G is the antenna gain, and T_{sys} is the system noise temperature. The optimal value can be determined by optimizing the aperture efficiency, which is achieved by balancing two key components: "taper efficiency" and "spillover efficiency" [5]. Both of these are expressed as functions of the edge taper T_e, defined as the ratio of the field intensity at the edge of the reflector to the field intensity at the reflector center. This balance ensures effective illumination of the reflector, minimizing energy loss while maximizing performance. Typically, the edge taper is set at $T_e \approx -11$ dB, a value widely recognized as an ideal compromise for achieving high aperture efficiency.

For Phased Array Feed systems, optimal illumination of the reflector is achieved by adjusting the complex weights of individual array elements and shaping the beams from the sub-arrays to match the dish's dimensions. To avoid under-illumination from narrow beams, each antenna element must produce a sufficiently wide beam for uniform coverage when sub-array beams are combined.

The Italian National Institute for Astrophysics (INAF) has made significant advancements in Phased Array Feed technology, giving a substantial contribution to the state of the art with the development and testing of the PHAROS and PHAROS2 systems [8,10–12]. The Italian National Institute of Astrophysics also manages the Sardinia Radio Telescope (SRT), a multiple reflector antenna with a large main mirror (64 m of diameter): in particular, simulations performed with the PHAROS2 Phased Array Feed placed in the primary focus (the distance between primary focus F1 and Gregorian Focus F2 is 17.4676 m [13]) of Sardinia Radio Telescope revealed that, at certain frequencies, the antenna efficiency drops to low levels [10]. This issue was attributed to under-illumination of the reflector caused by the narrow beams generated by a combination of 13 equally weighted antenna elements. Consequently, the system failed to adequately illuminate the Sardinia Radio Telescope dish, reducing overall system performance.

To address this limitation, a new room-temperature Phased Array Feed demonstrator with a new dedicated antenna is currently under development [14–16]. This next-generation instrument operates within the C-Band frequency range (4.75–6.00 GHz) and it is designed to be upgradable, covering a wider frequency range, from 3.0 to 7.7 GHz. In this work, we present the design of the new antenna for the demonstrator, which consists of an 8×8 array of dual-polarized unit cells. The single antenna element has been carefully optimized to achieve a uniform beam pattern across the extended operational frequency range and an edge taper significantly wider than the single radiating element of PHAROS2. Specifically, the design provides an edge taper of approximately -5 dB in the E-plane or H-plane

over the 3.0–7.7 GHz frequency band. This will ensure efficient reflector illumination, allowing the Phased Array Feed to contribute to the formation of the compound beam, and overcomes the limitations identified in the PHAROS2 system, enabling improved performance across the C-Band.

This paper describes in detail a novel approach to design a Phased Array Feed antenna using a reverse design strategy. Unlike traditional methodologies, which prioritize optimizing the Active Reflection Coefficient (ARC) to minimize signal reflections and ensure good impedance matching across the operating bandwidth and beam-pointing directions, this method focuses on optimizing the radiated field. The innovation of this approach lies in redefining the primary design goal: achieving a specified edge taper (−5 dB in this case) at a designated angle (140° here) in the E-plane or H-plane across the entire frequency range. This reverse strategy shifts the emphasis from Active Reflection Coefficient and impedance matching to superior field performance, making it particularly well-suited for the demanding requirements of radio astronomy applications.

The proposed antenna was designed using CST® Microwave Studio 2020, a leading software for 3D electromagnetic simulation of microwave components. Over the last two decades, CST has proven to be a reliable tool in the electromagnetic community, with simulation results closely matching experimental results both for the radiating performance and for the evaluation of the scattering parameters [17–22]. Fabricating the Phased Array Feed array is complex and requires advanced technologies and infrastructure that are currently unavailable to us. Therefore, we utilized CST® Microwave Studio to evaluate the Phased Array Feed's performance, ensuring accurate assessments through its robust simulation capabilities. This innovative design aims to enhance performance compared to earlier configurations [6,7,10,23,24], offering increased sensitivity, broader frequency coverage, and improved beam-shaping capabilities. Ultimately, this leads to greater survey efficiency and an expanded Field of View (FoV). The development of advanced phased array feeds like the proposed C-Band Phased Array Feed marks a significant advancement in radio astronomy instrumentation, improving observational capabilities and facilitating more efficient large-scale surveys of the universe.

2. Antenna Design

This section outlines the design of a new C-Band Phased Array Feed antenna for the Sardinia Radio Telescope, covering a frequency range of 3–7.7 GHz. The antenna consists of an 8 × 8 array of 64 dual-polarized unit cells, resulting in a total of 128 radiating elements. Only the central 32 unit cells will connect to the backend system, while the remaining will be terminated with 50 ohm passive loads (Figure 1). This setup allows simultaneous generation of multiple independent beams through digital selective sub-array activation [14–16].

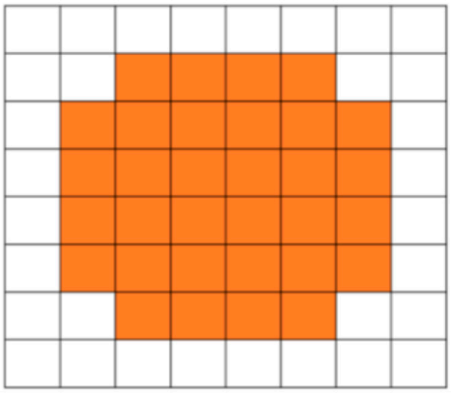

Figure 1. Simplified layout of the 64-element array, showing the central 32 active elements highlighted in orange.

The design approach for the antenna unit cell outlined in this work differs significantly from traditional phased array design methods, which typically optimize the Active Reflection Coefficient to ensure minimal signal reflections and good impedance matching across the operating bandwidth and for various beam pointing directions.

The key steps in our design procedure can be summarized as follows:

- **Reverse design strategy:** unlike conventional approaches that prioritize impedance matching, this work adopts a reverse design strategy, starting with radiated field optimization. In our case, the primary design goal is to achieve, for the single antenna of the array, a -5 dB edge taper at a 140° angle in either the E-plane or H-plane across the full 3–7.7 GHz frequency band. To meet this requirement, both the single unit cell and the finite array model are used. Specifically, only one element of the finite array is fed during the simulation to analyze and optimize the radiated field performance;
- **Unit cell Active Reflection Coefficient optimization:** thanks to periodic boundary conditions, this approach assumes an infinite array which provides a reliable approximation for large arrays, such as the 8×8 configuration considered in this work. The Active Reflection Coefficient (ARC) and the active element radiation pattern are computed for the antenna within this infinite array model [25]. For relatively large arrays, where edge elements have minimal influence on the overall performance, this method effectively represents the array behavior with a limited computational cost [26]. In Phased Array Feed designs for radio astronomy applications, the optimization process focuses specifically on the scanning angle relative to the broadside direction as a function of the frequency [6,7,23,27]. This ensures that the antenna element delivers optimal impedance matching and minimal signal reflections across the desired operational bandwidth;
- **Finite array and pattern analysis:** once an acceptable Active Reflection Coefficient is achieved, the finite array is analyzed. In this step, edge elements are evaluated and, if necessary, adjusted so their impedance closely resembles that of the infinite array. This step also involves examining the array radiated field patterns, beamwidth, side lobe levels, and edge taper.

2.1. Single Antenna Design

In the development of Phased Array Feeds for radio astronomy, the single radiating element is usually an Exponential Tapered Slot Antenna (ETSA), commonly known as the "Vivaldi" antenna [6,7,28,29]. These antennas are preferred because of their wide bandwidth, straightforward fabrication, good impedance matching, reasonable gain, and cost-effectiveness [9,30–33].

In this work, we diverge from the conventional exponential taper profile and instead utilize a linear taper profile, implementing each antenna element on a metallic structure. This design choice provides three key advantages: a broad operating bandwidth, wider beam width [34], and enhanced compatibility with radio astronomy cryogenic applications where low background noise are required. Metallic structures exhibit excellent electrical conductivity and thermal stability both at cryogenic and room temperatures if compared to any radiated structure made on substrate: these aspects ensure that the Phased Array Feed maintains high sensitivity—a critical factor for high-performance radio astronomy receivers. However, the proposed antenna will be a part of a new C-Band PAF demonstrator designed to operate at room temperature without requiring a cryostat, as detailed in [14–16]; for this reason, in this work, we may overlook considering aspects related to the antenna's behavior under extreme environmental conditions, such as cryogenic temperature fluctuations.

The single Linear Taper Slot Antenna of the array consists of two main sections: the propagation and the radiation section (Figure 2). The first one guides the signal toward the open end, and the second one influences the operational bandwidth [35].

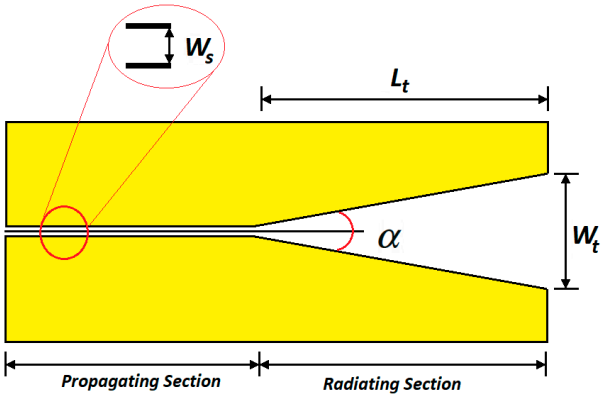

Figure 2. Diagram of a typical Linear Tapered Slot Antenna with key parameters, such as taper length (L_t), opening angle α, taper width (W_t), and feed slot width (W_s), clearly marked.

The choice of a Linear Taper Profile rather than an exponential one is based on performance considerations: a Linear Taper Profile Antenna is less sensitive to variation in the aperture angle [36], making it advantageous for the optimization of edge taper in the design process. The geometric parameters of the antenna are as follows:

- **Taper length** (L_t): directly affects the bandwidth of the antenna. A longer taper length allows the electromagnetic field to transition more gradually from the feed to the radiating end, resulting in improved directivity and a broader operational frequency range [34];
- **Opening angle** α: determines the antenna shape and aperture, influencing its radiation pattern. Typical values for the opening angle range from 5° to 12° [34]. The taper shape is mathematically described by the following linear equation:

$$y = ax + b \tag{1}$$

where a and b are constants derived from the start and end points of the taper. The opening angle α is twice the slope of the line in the Equation (1), placing the origin of a Cartesian orthogonal reference system in the center of feed slot width. We can write $\alpha = 2 \times a$;

- **Taper width** (W_t)**:** the taper width, measured at the open end of the antenna, is typically designed using the following formula:

$$W_t = \frac{1}{2} \cdot \frac{c}{f_{min}} = \frac{1}{2}\lambda_{max} \tag{2}$$

where f_{min} is the lowest frequency in the antenna operational range. The taper width, along with the opening angle, determines the effective radiating aperture of the antenna;

- **Feed slot width** (W_s): the feed slot width is critical for achieving optimal impedance matching between the feed line and the radiating aperture.

The layout is shown in Figure 2, where all the parameters are clearly depicted. Each of these design aspects contributes to the antenna's ability to deliver high efficiency, broad bandwidth, and tailored radiation characteristics.

2.2. Infinite Array Approximation

Integrating Linear Tapered Slot Antenna elements into a phased array poses additional challenges compared to their standalone operation, primarily due to the element spacing,

which directly influences the array's ability to form and steer beams without introducing grating lobes or other distortions. In phased arrays, the spacing W_p between adjacent elements (Figure 3) is typically set between 0.4 and 0.5 λ_{min}, where λ_{min} is the wavelength at the highest operating frequency [37,38]. Consequently, the taper width W_t must also remain smaller than 0.5 λ_{min}. This spacing adheres to the Nyquist criterion, preventing spatial aliasing and ensuring the integrity of the beamforming process.

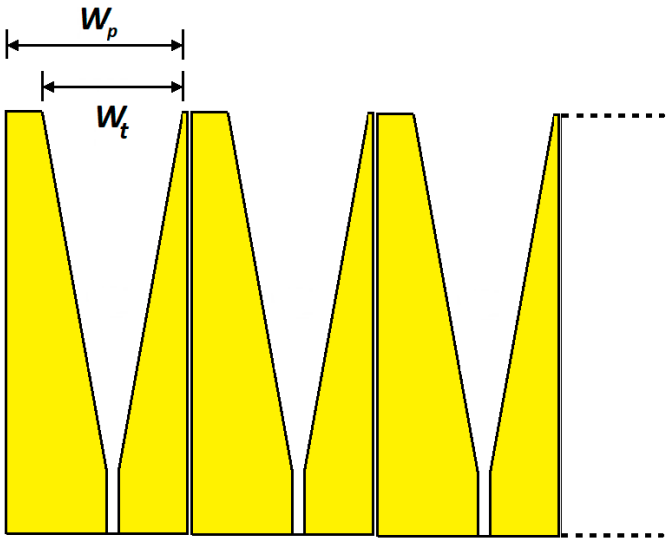

Figure 3. Spacing between adjacent elements of the array.

Unlike standalone antennas, individual elements within a phased array are subject to mutual coupling effects, which arise from the electromagnetic interactions between neighboring elements. These interactions can significantly alter the antenna input matching, reduce radiation efficiency, and degrade overall array performance. Such effects are particularly detrimental in applications requiring precise beam steering and high sensitivity, such as radio astronomy. Therefore, optimizing the performance of a phased array, particularly in terms of input impedance matching and radiation characteristics, cannot rely solely on simulations of isolated antenna elements in free space.

To address these challenges, an isolated element with a taper width ranging from 0.4 to 0.5 λ_{min} was initially simulated in free space. While this setup demonstrated acceptable impedance matching, the bandwidth performance was limited due to the absence of neighboring elements and mutual coupling effects. To better understand the antenna behavior in a large array configuration, we use the "unit cell" infinite array approximation. This method models an infinite periodic array, with each antenna element surrounded by identical ones, repeating periodically in the directions identified by the array plane. The infinite array approximation allows for the analysis of the mutual coupling effect in large arrays, where central elements experience uniform interactions from their immediate neighbors. The "unit cell" technique has been adopted in the design of large-scale phased arrays [25,39,40] and Phased Array Feeds (PAFs) for radio astronomy [7,23,27], offering a practical and accurate framework for evaluating phased array performance, particularly in applications like radio astronomy, where a precise modelling of mutual coupling is crucial.

2.3. Unit Cell Characteristics and Initial Settings

This section describes the unit cell geometry, key parameters, and the rationale for their selection. The design must comply with the Nyquist sampling criterion while ensuring a wide operational bandwidth from 3 to 7.7 GHz. Critical parameters like element spacing (*Wp*) and taper length (*Lt*) were carefully chosen, with initial settings established as follows:

- **Element spacing $W_p = \lambda_{min}/2 = 19.48$ mm**: where λ_{min} is the wavelength corresponding to the highest frequency (7.7 GHz). This spacing adheres to the Nyquist sampling criterion, ensuring the prevention of grating lobes in the array radiation pattern across the wide frequency range. By maintaining the selected value of W_p throughout the unit cell optimization process, the risk of grating lobes across the frequency range is effectively minimized, which is essential for preserving the array performance at higher frequencies;
- **Taper length $L_t = \lambda_{max}/2 = 50$ mm**, where λ_{max} corresponds to the wavelength at the lowest frequency (3 GHz). Unlike W_p, L_t is optimized to meet specific edge taper and bandwidth requirements. Adjustments to L_t, and consequently the opening angle α, play a significant role in shaping the radiation beam characteristics to achieve a consistent and desirable edge taper across the entire operational bandwidth.

To balance structural integrity and compactness, the radiating walls of the unit cell are constructed with a metal thickness of 3 mm. This size ensures sufficient mechanical stability while maintaining a lightweight and compact design, which is a crucial aspect for the dense antenna arrangement required in the Phased Array Feed array.

The unit cell design employs a dual-polarized configuration with two orthogonally positioned Linearly Tapered Slot Antennas. Each antenna operates independently, enabling the unit cell to accommodate two orthogonal polarizations:

- **Horizontal polarization:** one element in each unit cell is oriented to radiate in the horizontal plane, efficiently capturing signals aligned with this polarization;
- **Vertical polarization**: the second element is aligned to radiate in the vertical plane, enhancing the unit cell dual-polarization capability.

Arranging the antennas with a 90-degree rotation relative to each other minimizes cross-polarization interference, crucial for signal integrity [26]. The orthogonal configuration (Figure 4a) enhances the detection of faint signals in both polarizations: this aspect is vital for radio astronomy applications.

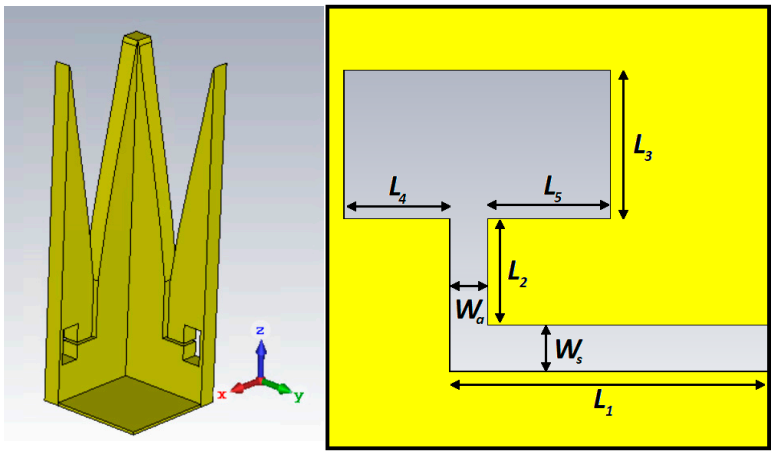

(**a**) (**b**)

Figure 4. (**a**) Unit cell; (**b**) parameters of the feeding network.

The feeding network of each individual antenna in the array plays a critical role in ensuring proper impedance matching across the entire operational frequency band. The propagation section is designed as an "L"-shaped slot, optimized with seven tunable parameters, as illustrated in Figure 4b. This design enables precise control on the antenna impedance characteristics to maintain efficient energy transfer within the wide frequency range.

Each antenna of the unit cell is fed using a 50 ohm integrated coaxial cable, which employs air as the dielectric medium. To embed this feeding structure within the antenna, a cylindrical channel with a diameter d = 1 mm is milled directly into the antenna body. This innovative approach seamlessly integrates the coaxial feed into the antenna structure, eliminating external attachments and their associated challenges. The antenna fabrication process involves manufacturing it in two distinct parts. One part is designed to house the coaxial probe, which is then inserted into the other part. This assembly approach simplifies the precise alignment of the central conductor of the coaxial cable within the milled channel, significantly reducing the risk of assembly errors. By eliminating the need for soldering, this design minimizes potential mechanical failures and prevents impedance mismatches caused by misaligned or incorrectly positioned external coaxial cables.

The central conductor of the coaxial feed has a diameter of 0.435 mm, which is carefully selected to ensure compatibility with the antenna impedance requirements. Figure 5 provides a detailed depiction of the coaxial feed probe integration, highlighting the cylindrical channel milled into the antenna structure to facilitate precise and seamless assembly.

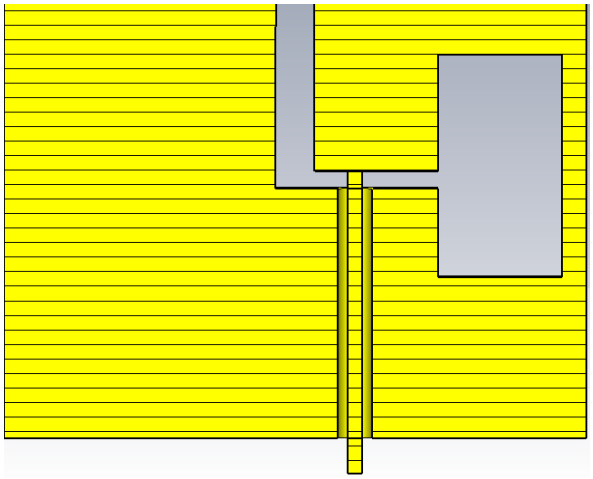

Figure 5. Implementation of the feeding probe integrated in the antenna.

Alternative solutions using 50 ohm integrated coaxial cables with larger diameters (i.e., 1 mm inner and 2.3 mm outer) have been tested, but here we present only the least dimensionally impactful option. We have ruled out a solution with the standard coaxial cable because the antenna array will be part of a more complex receiver [14–16], and we plan to connect it directly to a pre-amplification board not detailed in this work.

2.4. Phased Array Feed Antenna Design

The first step in designing the Phased Array Feed antenna involves optimizing the geometrical parameters of the unit cell antenna (Figure 2) to achieve a -5 dB edge taper in the E-plane or H-plane at a 140° angle, over the operational frequency range from 3 to 7.7 GHz. To meet this requirement, an extensive series of parametric simulations was conducted to optimize the radiated field. The proper impedance matching between the unit cell and the external feeding network will be performed in the last step of the design process. In our approach, the Phased Array Feed antenna design represents a careful balance between achieving the desired beamwidth and maintaining impedance matching across the required frequency band

While adjusting the beam radiated by a single antenna, it is crucial to account for mutual coupling effects caused by the interactions with neighboring elements in the array. To address this, a 128-element array was introduced as a “raw” prototype of the Phased

Array Feed antenna. The layout of this phased array feed, with dual-polarized capabilities, is illustrated in Figure 6a.

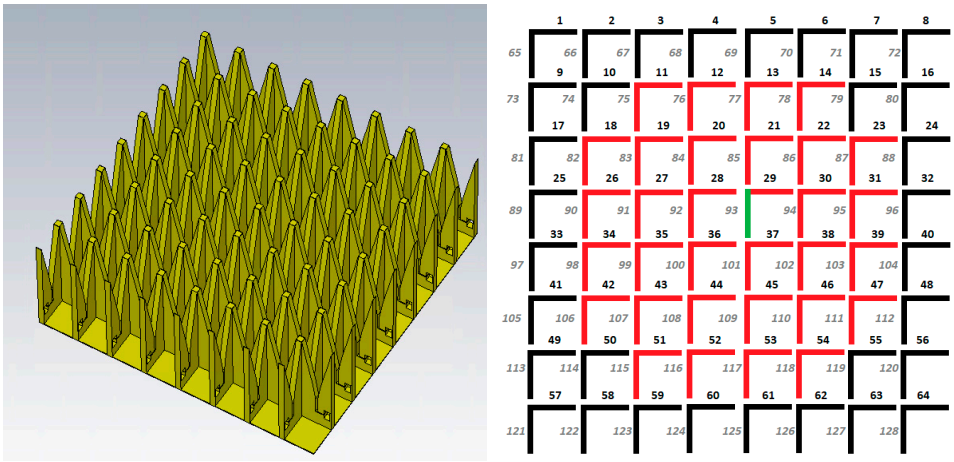

(**a**) (**b**)

Figure 6. (**a**) 3D view of the 128-element array; (**b**) antenna feeding scheme for edge taper adjustment (in red color the active zone): the antenna numbered with 93 and highlighted in green is the only one that is powered.

The edge taper optimization was performed through a selective activation procedure, where only specific elements in the active zone were fed, while others were connected to passive loads. Figure 6b illustrates the feeding configuration for the active zone, activating the antenna element 93 at the center of the array grid. The selection of element 93 for the edge taper optimization process is intentional, strategic, and carefully considered. Located at the center of the array grid, this element experiences the maximum level of interaction with the surrounding antennas. This central position makes it the most representative choice for evaluating and optimizing the edge taper, as it accounts for the cumulative influence of neighboring elements.

In this initial phase of the design process, our primary focus is on achieving the desired edge taper without introducing additional variables. Once this objective is successfully met, we will conduct a thorough evaluation of mutual coupling levels across the array. If these coupling levels are found to be excessively high, all the necessary adjustments will be made to address and mitigate their impact and ensure the overall stability and performance of the system.

The procedure is not directly related to beamforming process: the proposed antenna will be the front-end of a new C-Band PAF demonstrator [14–16], where the beamforming will be managed by a digital backend based on a Xilinx ZCU216 RFSoC board. All the beamforming processes are therefore achieved in the post-processing stage: this means that from an electromagnetic modelling point of view, each single element of the active zone can be considered as connected to identical current sources with the same phase and amplitude.

The edge taper specifications were achieved by adjusting the taper length L_t and, consequently, the opening angle α of the single antenna. In Linear Taper Slot Antennas, the angle α typically ranges from 5° to 12°, and it directly influences the width of the radiated field [34]. For isolated antennas, when the ratio $L_t/\lambda_0 \leq 2$ (where λ_0 is the free-space wavelength), the radiated beamwidth increases significantly in both the E-plane and H-plane [34,36]. Additionally, L_t is proportional to the operational bandwidth [32]; therefore, in this study, taper lengths exceeding λ_{max} were avoided to prevent an excessively large radiant structure.

Different values of L_t were tested to determine the optimal configuration. In all simulations, both the elements spacing W_p and the width W_t are constant and equal to 19.48 mm and 16.48 mm, respectively. The parameter W_p can be indeed calculated as the difference between the element spacing W_p and the thickness of metal employed for the antenna manufacturing (see Figures 3 and 4a). As shown in Figure 7, the opening angle α increases for decreasing values of taper length L_t (as apparent when looking at Figure 2, where the geometry of the structure is depicted). Consequently, the radiated field beamwidth narrows progressively in the H-plane when L_t decreases. This relationship demonstrates how taper length adjustments directly influence the beamwidth, enabling fine-tuning of the edge taper for optimal performance.

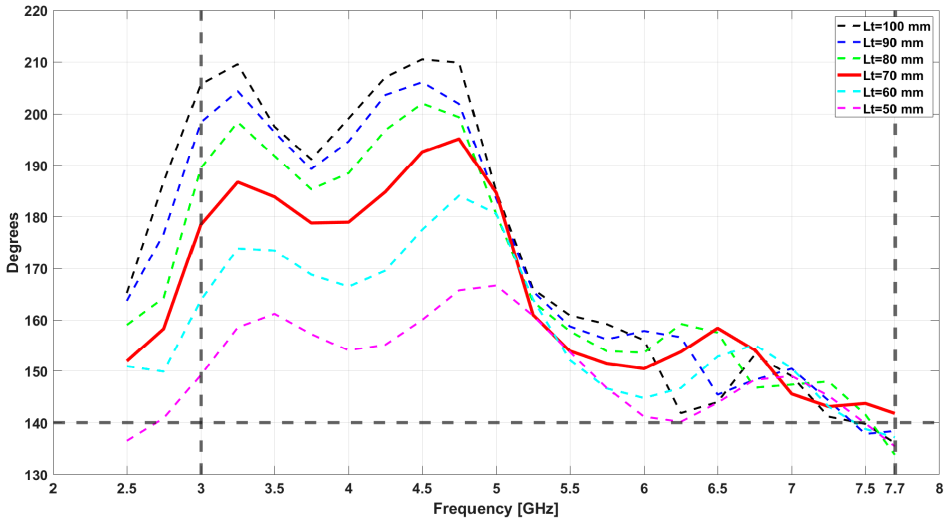

Figure 7. H-plane 5 dB edge taper: variation of taper length L_t.

The variation in the taper length L_t has a pronounced impact on the edge taper in the H-plane, particularly for frequencies below 5.25 GHz. In this range, the taper width is highly sensitive to changes in L_t. However, for frequencies between 5.25 GHz and 7.7 GHz, this effect becomes less significant, with the edge taper stabilizing between 140° and 160°. In contrast, in the E-plane, the edge taper shows minimal sensitivity to variations in L_t, remaining consistently below 140° for frequencies above 3.5 GHz, as shown in Figure 8.

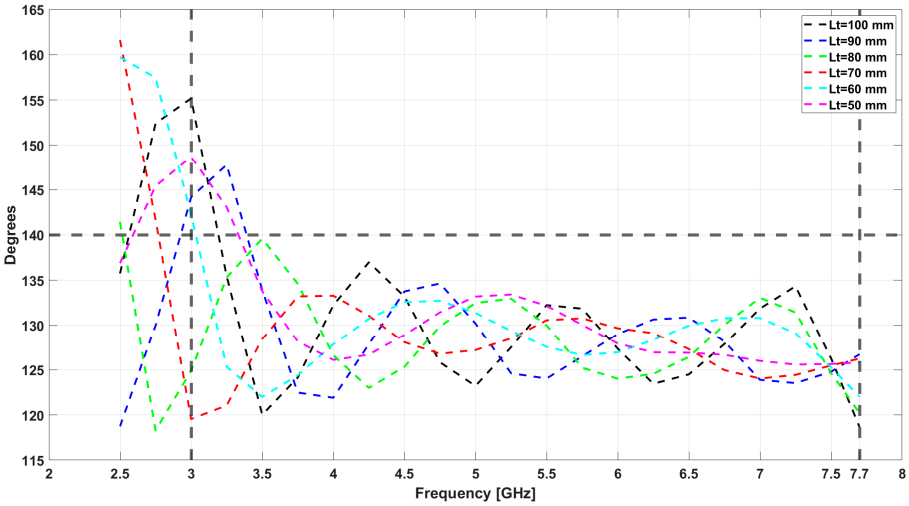

Figure 8. E-plane 5 dB edge taper: variation of taper length L_t.

The design specifications for the H-plane are met when L_t = 70 mm, corresponding to an opening angle α = 6.325°. This configuration ensures a −5 dB edge taper greater

than 140° across the entire frequency range of 3 to 7.7 GHz. Figures 9 and 10 present the normalized simulated radiation patterns of the single powered Linear Tapered Slot Antenna in both the H-plane and E-plane at frequencies of 3 GHz, 5.5 GHz, and 7.7 GHz, demonstrating the optimized radiation performance.

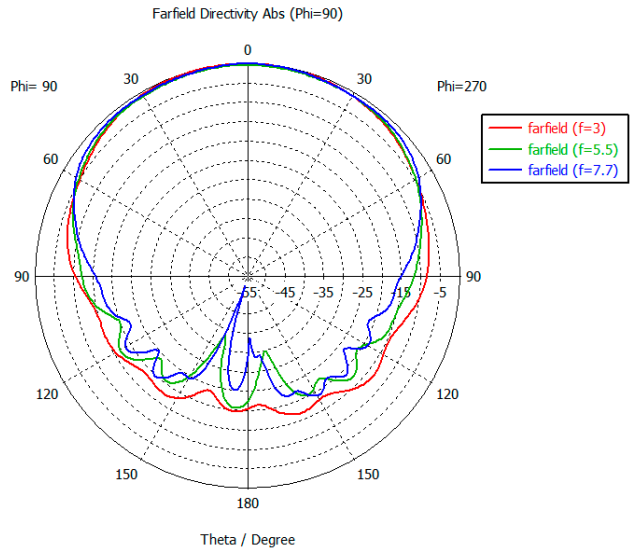

Figure 9. Single Linear Tapered Slot Antenna H-plane-normalized radiated field.

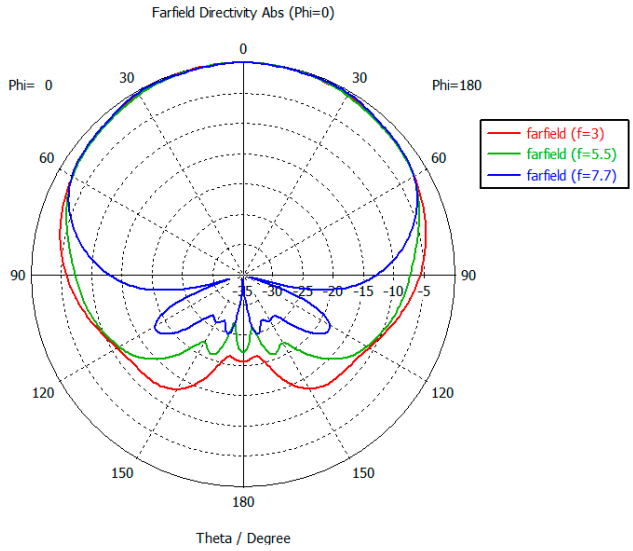

Figure 10. Single Linear Tapered Slot Antenna E-plane-normalized radiated field.

The comparison between the obtained −5dB edge taper of the single Linear Tapered Slot Antenna of the Phased Array Feed antenna and the one of the single elements of the PHAROS2 antenna is reported in the Figures 11 and 12.

The results obtained in the 4–7 GHz frequency range show that the radiated field of the single antenna in the array exhibits an edge taper in the H-plane that is significantly improved with respect to single element of the PHAROS2 antenna. In the E-plane, the edge taper that is achieved remains almost constant in a range of values between 122 and 133°.

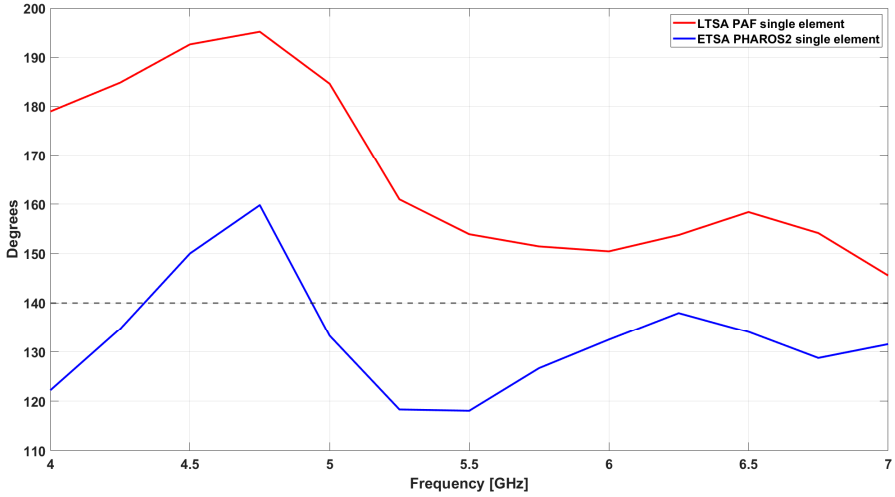

Figure 11. The −5 dB H-plane edge taper comparison.

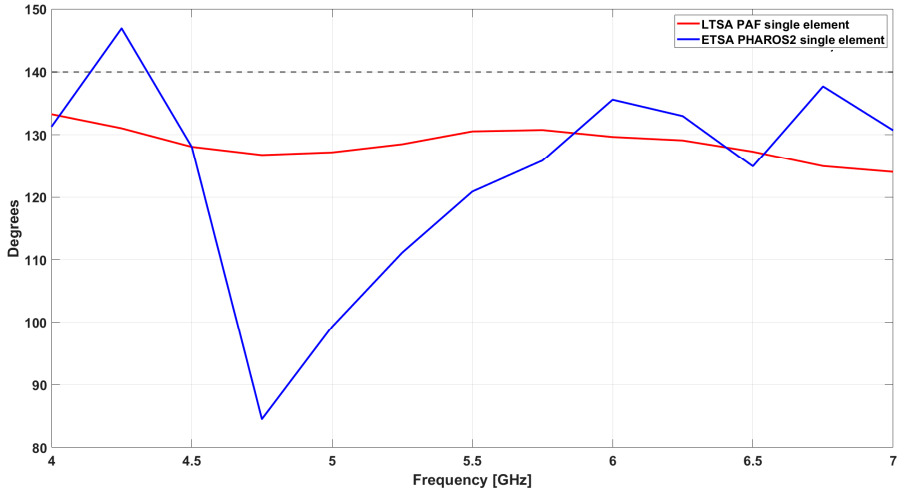

Figure 12. The −5 dB E-plane edge taper comparison.

With the radiated field successfully optimized to achieve the required edge taper, the next design step focuses on refining the Active Reflection Coefficient to ensure proper impedance matching. This step employs an infinite array model (described in the previous section as the unit cell array approach) to align the antenna performance with the feed network requirements. Using the optimized L_t value obtained in the previous step (L_t = 70 mm), care was taken to preserve the radiated field configuration while fine-tuning the slot widths and parameters of the "L-shaped" slot to achieve optimal impedance matching across the 3–7.7 GHz frequency band (refer to Figure 4b for the antenna geometry). Key geometric parameters of the optimized unit cell include the following: L_1 = 7.5 mm, L_2 = 3.5 mm, L_3 = 3.5 mm, L_4 = 2.5 mm, L_5 = 3.3 mm, W_a = 0.5 mm, and W_s = 1.1 mm, whereas the total length of the single radiating element along the z-axis is 87 mm. The geometries of the optimized unit cell and its feeding network are reported in Figure 13a and 13b, respectively. The insertion point of the probe is located at 1.95 mm from the upper edge of the feed slot (see Figure 13b). The optimized unit cell exhibits excellent performance, achieving an Active Reflection Coefficient below −12 dB across the operational bandwidth and below −14 dB in the frequency range of 3 to 7.2 GHz, the mutual coupling between the two orthogonally polarized elements of the unit cell is below −24 dB, as shown in Figure 14.

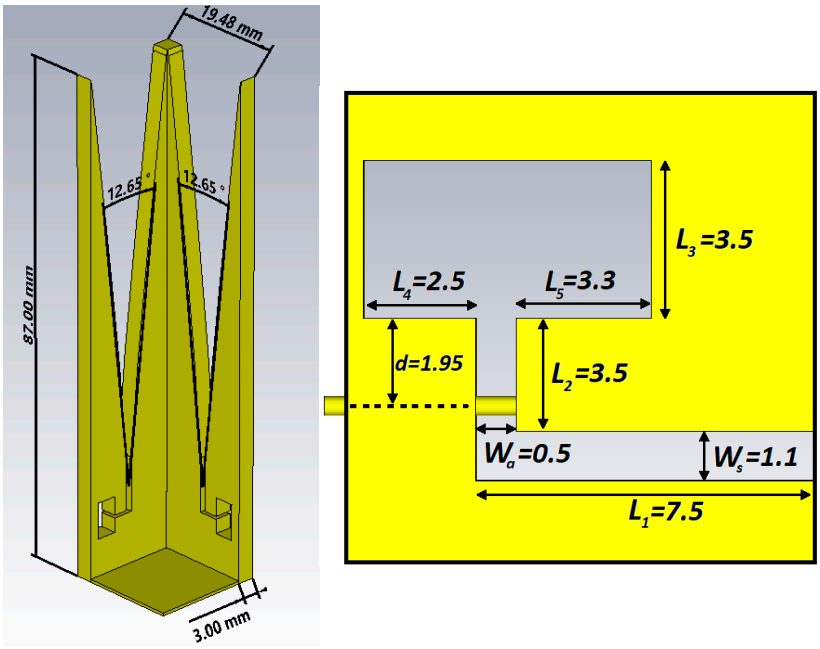

(**a**) (**b**)

Figure 13. (**a**) Overall dimensions of the optimized unit cell, and (**b**) optimized parameters of the "L-Shaped" slot: all dimensions are in millimeters.

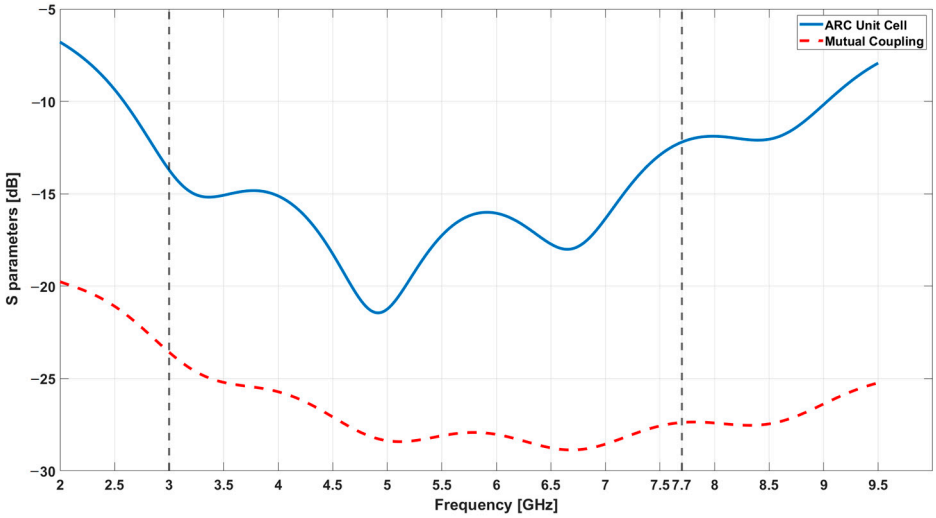

Figure 14. S-parameters of the dual-polarized unit cell.

Throughout the simulations conducted during the design process, deliberate variations of a few hundredths of a millimeter from the optimal dimensions were introduced. This approach was adopted to account for potential manufacturing tolerances and inaccuracies that could arise during the production phase of the antenna. The results demonstrated that these slight deviations had no significant impact on the performance of the design, specifically in terms of edge taper and Active Reflection Coefficient (ARC). This holds true for both the Linear Taper Slot Antenna (LTSA) and the unit cell, confirming the robustness of the proposed design against minor fabrication imperfections.

To account for edge effects and further validate the design, a finite array model was created by adding 16 additional passive elements along the two open sides of the array, increasing the total number of antennas to 144. The resultant array has a size of 158.84 × 158.84 × 87 mm. This configuration is depicted in Figure 15, which illustrates the

strategic placement of the additional elements to form an artificial buffer zone along the array boundaries.

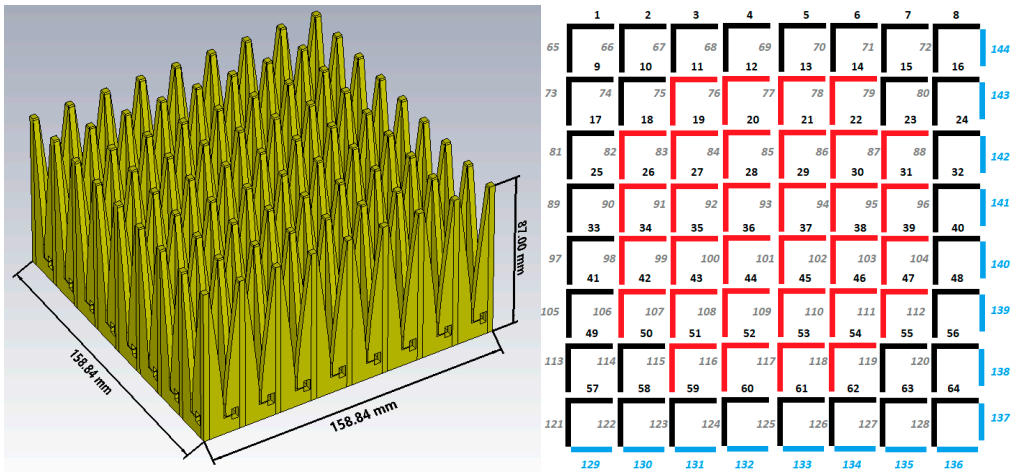

(**a**) (**b**)

Figure 15. (**a**) Finite array model with additional boundary elements, and (**b**) the antenna feeding scheme for the final configuration of the Phased Array antenna: the 16 passive additional elements are highlighted in blue color. In red color is the active zone.

By incorporating these boundary elements, the active antennas near the center of the array exhibit an Active Reflection Coefficient that closely resembles that of the isolated unit cell. Figure 16 compares the Active Reflection Coefficient of antenna 93 (located at the center of the array) with that of the unit cell, demonstrating excellent agreement. It is worth noting that the results for the edge taper remain consistent with those shown in Figures 7 and 8, confirming that the addition of boundary elements does not compromise the radiated field performance.

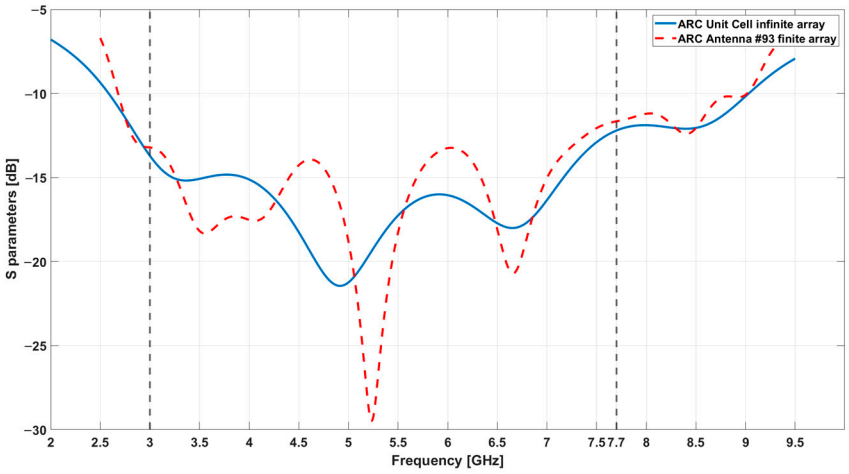

Figure 16. Comparison between the Active Reflection Coefficients of the single antenna of the unit cell and the antenna labelled with number 93 in the finite array.

Referring to the antenna feeding scheme illustrated in Figures 15b, 17 and 18 show the mutual coupling level between the central element (labelled with the number 93) and some elements of the array having the same polarization or in a 90° configuration, including antennas located at the edge of the active region: as expected, the antenna's mutual coupling tends to decrease as the distance between the elements increases.

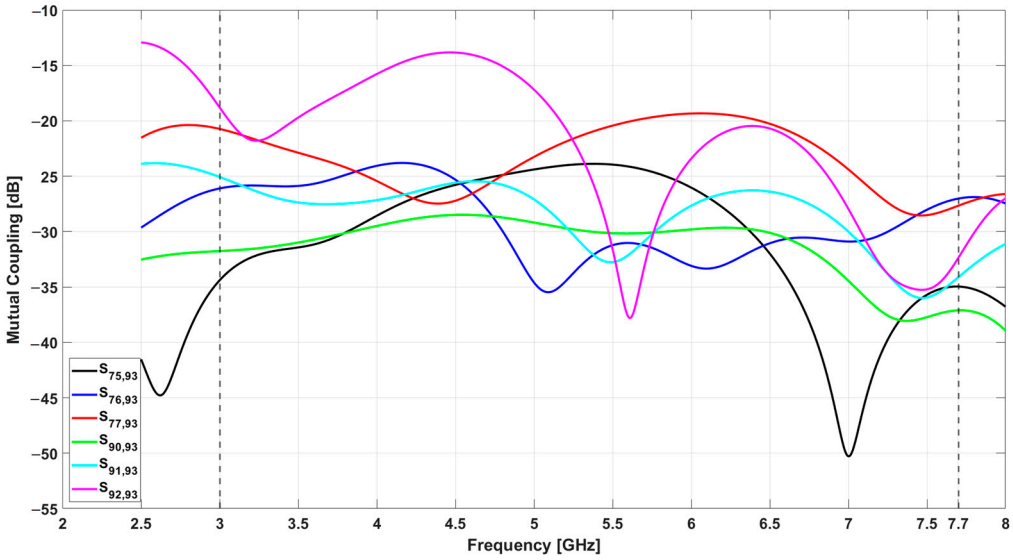

Figure 17. Simulated mutual coupling between some elements having the same polarization.

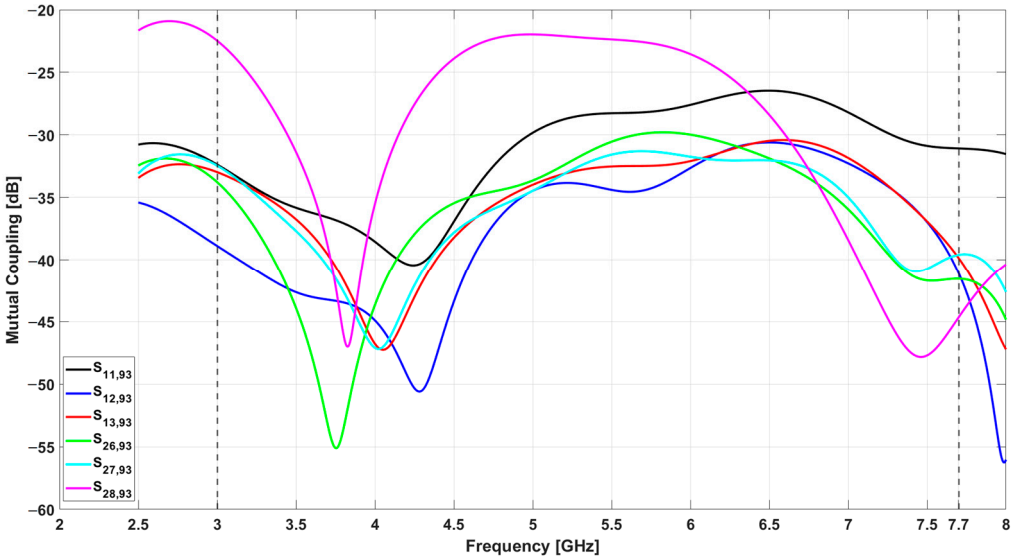

Figure 18. Simulated mutual coupling between some elements having cross-polarization.

The performances and the methodology design of the proposed Phased Array antenna are compared with the recent literature in Table 1. The achieved results and main limitations of each paper referenced in the Table are summarized below.

Ref. [6] provides a comprehensive experimental evaluation and detailed performance of both isolated antennas and elements within an array. Mutual coupling between co-polarized elements ranges from −21 to −28 dB (peaking at −30 dB), with a single-element gain of 6–7 dB. The beamwidths are 40° (E-plane) and 50° (H-plane), with sidelobe levels of 13.5 dB and 21.4 dB, respectively. The main limitation is due to the use of Exponential Tapered Slot Antenna elements with a large element pitch (50 mm), resulting in reduced bandwidth (3–6 GHz) and potential grating lobe issues.

Table 1. Performance comparison.

Reference	Frequency Band [GHz]	Single Element	Single Element Pitch [mm]	Single Element Length [mm]	Array Elements	Design Procedure	Optimization of the Array Single Element Edge Taper
This work	**3–7.7**	**LTSA**	**19.48**	**87**	**144**	**Unit cell–infinite array**	**Yes**
[10] *	4–7	ETSA	21	77	220	Unit cell–infinite array	No
[6]	3–6	ETSA	50	116	320	Unit cell–infinite array	No
[7]	2.8–5.18	ETSA	28.8	53.6	140	Unit cell–infinite array	No
[23]	2.5–4	ETSA	37	125	40	Unit cell–infinite array	No
[24]	4–8	Bowtie	25	18.75	24	Standalone antenna	No
[41] **	1.3–1.72	Bowtie	135	13	69	NA	No
[42]	15.4–20.0	SIW	8.98	19.6	24	Unit cell–infinite array	No
[43]	2.5–4	DRA	30	NA	253	Standalone antenna	No
[44]	0.65–1.45	ETSA	125	125	90	Standalone antenna	No
[45]	0.7–1.8	ETSA	30.025	161	220	NA	No

* Performance data for the unit cell are available in [46]. ** For more details of the array single element see also [47].

In [7], numerical results are reported for the reflection coefficient for infinite and finite arrays, but it lacks data on mutual coupling, and beam characteristics are unclear due to scaling issues in radiated field plots. Therefore, it provides insufficient details on practical array performance.

Ref. [10] reports simulated results and analysis of a PHAROS2 Phased Array Feed coupled with the Sardinia Radio Telescope (SRT) primary mirror and includes plots of individual antennas, a 13-element beam, and the Sardinia Radio Telescope illumination by the composite beam, with a gain of ~6 dB for a single antenna. It focuses on system-level coupling rather than individual antenna design improvements, lacking details on mutual coupling and array performance, such as edge taper optimization and grating lobe suppression.

Ref. [23] presents both the reflection coefficient and mutual coupling experimental data for a finite array, with return loss below −10 dB for all elements and cross-coupling better than −20 dB for same-polarization elements. The proposed Phased Array Feed operates within a narrow band (2.5–4 GHz) and lacks single-antenna field data.

Ref. [24] discusses the standalone Bowtie antenna design without unit cell simulations, reporting the numerical data for the reflection coefficient and mutual coupling for the isolated antenna. The presented antenna covers the 4–8 GHz range, but the paper does not analyze any array configuration or edge taper optimization.

In [41], a simulated Bowtie array is described, but the paper provides only basic information, such as the number of antennas and the operating frequency band (1.3–1.72 GHz).

Other critical performance metrics, such as mutual coupling or radiated fields and beam patterns, are missing.

Ref. [42] evaluates a small-scale array with simulated values of the reflection coefficient of the unit cell, showing a mutual coupling below −20 dB for the infinite array. While it provides acceptable simulations, the small scale limits its applicability to larger arrays. Moreover, it is focused on a small array, and no radiated field data for the single antenna element are given.

Ref. [43] discusses the numerical data for the array bandwidth (2.5–4 GHz) but lacks metrics on array performance, such as mutual coupling or beamwidths.

Ref. [44] is a standalone Exponential Tapered Slot Antenna design and focuses on single antenna performance. While it reports numerical data on the mutual coupling, though only for same-polarized elements, it lacks radiated field data for array elements. Moreover, the Active Reflection Coefficient has not been evaluated, and the simulated reflection coefficient of the finite array is significantly worse compared to the isolated antenna.

Finally, in [44], a low-frequency Exponential Tapered Slot Antenna Array is described. The paper reports basic specifications, including the size (30.025 mm pitch) and simulated bandwidth (0.7–1.8 GHz). However, it lacks array design details and radiated field data, without discussing antenna fields or band characteristics in detail.

It is apparent that our results represent a significant advancement over the state-of-the-art designs. The proposed antenna achieves an optimal combination of the widest operational bandwidth, compact element spacing, and a highly optimized single-element design (a Linear Tapered Slot Antenna). Moreover, our alternative design methodology, employing unit cell and infinite array simulations, enables arbitrary and detailed edge taper optimization. These features collectively enhance its beam-forming capabilities and adaptability to a wide range of applications. A detailed analysis of its performance trade-offs and advantages reveals the following key attributes:

- **Operational bandwidth:** The proposed design boasts the broadest operational bandwidth, surpassing conventional designs such as [6] (3–6 GHz) and [23] (2.5–4 GHz). This makes it particularly suitable for applications requiring high-frequency agility, such as radio astronomy. The extended bandwidth also facilitates use across multiple sub-bands, covering a range from 2.53 to 9 GHz;
- **Enhanced Design Methodology**: optimizes edge taper using unit cell simulations, providing a unique advantage and ensuring excellent and robust impedance matching and wideband performance. None of the references include this level of optimization;
- **Superior element choice:** employs Linear Tapered Slot Antenna elements, which deliver better broadband performance than traditional Exponential Tapered Slot Antennas ([6,7]) and compact Bowtie elements ([24]);
- **Grating lobes and beam quality:** with a smaller element pitch of 19.48 mm, this design effectively minimizes grating lobes, which is especially important for high-frequency and wide-angle operations. This feature delivers superior beam quality compared to larger pitches in [6] (50 mm) and [7] (28.8 mm);
- **Compactness and resolution:** the proposed antenna strikes an excellent balance between compactness and resolution, featuring a moderate array size of 144 elements. This provides adequate resolution while maintaining manageable system complexity. By contrast, ref. [6] achieves higher resolution with 320 elements but at the expense of increased size and processing demands;
- **Design innovation:** the use of Linear Tapered Slot Antenna elements optimizes the antenna for broadband performance, offering a distinct advantage over the more common Exponential Tapered Slot Antenna elements used in other designs such

as [6,7,23]. While Bowtie elements in [24] offer compactness, they are less effective for wideband applications;

- **Flexibility:** the combination of a smaller element pitch and a broad operational bandwidth makes this design highly versatile. It is capable of supporting additional frequency bands, outperforming narrower-band designs such as [7,23].

2.5. Numerical Simulations Methods, Settings, and Computational Resources

This study employs CST STUDIO Suite to perform electromagnetic simulations using two distinct approaches tailored to different problem scales. For the infinite array unit cell, a Frequency Domain Solver based on the Finite Element Method (FEM) is used. This setup applies periodic boundary conditions in the x and y directions and an open (add space) boundary with Floquet modes along the *z*-axis. An adaptive mesh refinement (AMR) strategy is executed over 16 equidistant frequency samples, with the refinement process halting when the absolute change in S-parameters falls below 0.001. Convergence was reached after 16 passes, resulting in a final mesh with approximately 42,583 tetrahedrons.

In contrast, the finite array configurations (128 and 144 elements) are simulated using the Finite Integration Technique (FIT) Time Domain Solver. Given the larger model size, open boundaries on all axes are applied, and the simulation begins with a heavy initial mesh (ensuring 2–3 mesh lines across critical gaps) followed by adaptive mesh refinement. The refinement continues until the change in S-parameters (ΔS) drops below -40 dB, with convergence achieved after five passes and a final mesh comprising roughly 345,974,720 tetrahedrons.

Both simulation strategies are executed on a high-performance workstation to manage the computational demands, ensuring numerical stability and high accuracy.

Table 2 summarizes the two simulation methodologies, defining the solver type used, the boundary condition, mesh refinement strategies, and the selected convergence criteria.

Table 2. Solver type, mesh refinement strategy, and convergence analysis.

Simulation Type	Solver and Approach	Boundary Conditions	Mesh Refinement Strategy	Convergence Criteria	Passes	Final Mesh
Infinite Array Unit Cell	Frequency Domain Solver (FEM)	Periodic (x,y); Open (z) with Floquet Modes	Adaptive refinement with 16 equidistant frequency samples	$\Delta S < 0.001$	16	~42,583 tetrahedrons
Finite Array configurations	Time Domain Solver (FIT)	Open boundaries along x,y,z	Heavy initial mesh ($\geq$2–3 lines across gaps) then AMR until $\Delta S < -40$ dB	$\Delta S < -40$ dB	5	~345,974,720 tetrahedrons

Table 3 outlines the high-performance computing environment used to efficiently handle the computationally intensive simulations, ensuring that both numerical accuracy and simulation speed are maintained.

Table 3. Computational resources.

Component	Specification
Processor	Dual AMD EPYC 7402 24-Core Processors @ 2.8 GHz
Memory	256 GB DDR4 ECC RAM
Operating System	Windows 10 Pro.

The rigorous CST simulations combine advanced solver techniques with an adaptive mesh refinement strategy and robust computational hardware, providing a reliable foundation for analyzing the LTSA Phased Array Feed.

3. Conclusions

This paper introduces the design and optimization of an innovative C-Band Phased Array Feed (PAF) antenna tailored for the Sardinia Radio Telescope (SRT). The antenna comprises an 8×8 array of dual-polarized elements, engineered to produce a uniform beam pattern and achieve an edge taper of approximately 5 dB for each radiating element within the 3.0–7.7 GHz frequency range. This advanced Phased Array Feed antenna overcomes key efficiency challenges identified in the PHAROS 2 system, including the inadequate illumination of the Sardinia Radio Telescope primary mirror due to the narrow radiation patterns of sub-arrays. The design methodology and finite array modeling presented in this work mark a significant advancement in Phased Array Feed (PAF) systems for radio astronomy. Departing from the conventional Active Reflection Coefficient-first design approach, this methodology prioritizes achieving precise edge taper control and optimizing radiated field characteristics before addressing impedance matching.

The integration of finite array modeling, enhanced with boundary elements to mitigate mutual coupling and edge effects, ensures consistent performance across the operational bandwidth. This tailored design strategy not only addresses the specific requirements of the Sardinia Radio Telescope but also establishes a robust framework for developing high-performance phased arrays in broader radio astronomy applications. It emphasizes precision in field characteristics and effective mutual coupling management, making it highly suited for the demanding performance standards of modern radio astronomy.

In conclusion, the proposed Phased Array Feed antenna sets a new benchmark in the field, offering unmatched performance across multiple parameters, making it an ideal candidate for demanding and versatile applications like radio astronomy.

Author Contributions: Conceptualization, P.M. and A.N.; methodology, P.M.; CST® EM simulations, P.M. and G.V.; validation, P.M. and G.A.C.; formal analysis, P.M.; data curation, P.M.; writing—original draft preparation, P.M. and G.A.C.; writing—review and editing P.M., G.A.C., G.M. (Giacomo Muntoni), and G.M. (Giorgio Montisci), supervision, A.N. and T.P.; project administration, A.N. and T.P. All authors have read and agreed to the published version of the manuscript.

Funding: This research received no external funding.

Data Availability Statement: The data presented in this study are available on request from the corresponding author.

Acknowledgments: We gratefully thank Andrea Melis (INAF) and Alessandro Cabras (INAF) for the OAC Data Elaboration Center hardware support in the heavy EM simulations. Special thanks to Pierluigi Ortu (INAF) for his logistical support.

Conflicts of Interest: The authors declare no conflicts of interest.

Abbreviations

The following abbreviations are used in this manuscript:

PAF	Phased Array Feed
SRT	Sardinia Radio Telescope
FoV	Field of View
PHAROS	PHased Arrays for Reflector Observing Systems
INAF	Italian National Institute for Astrophysics
OAC	Astronomical Observatory of Cagliari
ARC	Active Reflection Coefficient

TSA	Tapered Slot Antenna
ETSA	Exponential Tapered Slot Antenna
LTSA	Linear Tapered Slot Antenna
EM	Electromagnetic
SIW	Substrate Integrate Waveguide
DRA	Dielectric Resonant Antenna
NA	Not Available
FEM	Finite Element Method
FIT	Finite Integration Technique
AMD	Advanced Micro Devices

References

1. Ivashina, M.V.; Kehn, M.N.M.; Kildal, P.; Maaskant, R. Decoupling Efficiency of a Wideband Vivaldi Focal Plane Array Feeding a Reflector Antenna. *IEEE Trans. Antennas Propag.* **2009**, *57*, 373–382. [CrossRef]
2. Fisher, J.R.; Bradely, R.F. Full-sampling array feeds for radio telescopes. In Proceedings of the SPIE Astronomical Telescopes and Instrumentation, Munich, Germany, 3 July 2000. [CrossRef]
3. Warnick, K.F.; Maaskant, R.; Ivashina, M.V.; Davidson, D.B.; Jeffs, B.D. High-Sensitivity Phased Array Receivers for Radio Astronomy. *Proc. IEEE* **2016**, *104*, 607–622. [CrossRef]
4. Roshi, D.A.; Shillue, D.W.; Simon, B.; Warnick, K.F.; Jeffs, B.; Pisano, D.J.; Prestage, R.; White, S.; Fisher, J.R.; Morgan, M.; et al. Performance of a highly sensitive, 19-element, dual-polarization, cryogenic L-band phased array feed on the Green Bank Telescope. *Astron. J.* **2018**, *155*, 18. [CrossRef]
5. Goldsmith, P.F. *Quasi-Optical Techniques: Gaussian Beam Quasioptical Propagation and Applications*; Wiley-IEEE Press: Hoboken, NJ, USA, 1998; ISBN 978-0-780-33439-7.
6. Raid, E.W.; Ortiz-Balbuena, L.; Ghadiri, A. A 324-Element Vivaldi Antenna Array for Radio Astronomy Instrumentation. *IEEE Trans. Instrum. Meas.* **2012**, *61*, 241–250. [CrossRef]
7. Locke, L.; Garcia, D.; Halman, M.; Henke, D.; Hovey, G.; Jiang, N.; Knee, L.; Lacy, G.; Loop, D.; Rupen, M.; et al. CryoPAF4—A Cryogenic Phased Array Feed Design. In Proceedings of the SPIE Astronomical Telescopes and Instrumentation, Edinburgh, UK, 28 June–1 July 2016. [CrossRef]
8. Navarrini, A.; Scalambra, A.; Rusticelli, S.; Maccaferri, A.; Cattani, A.; Perini, F.; Ortu, P.; Roda, J.; Marongiu, P.; Saba, A.; et al. The Room Temperature Multi-Channel Heterodyne Receiver Section of the PHAROS2 Phased Array Feed. *Electronics* **2019**, *8*, 666. [CrossRef]
9. Gibson, P.J. The Vivaldi Aerial. In Proceedings of the 9th European Microwave Conference, Brighton, UK, 17–20 October 1979. [CrossRef]
10. Navarrini, A.; Nesti, R.; Schirru, L. Electromagnetic simulation and beam-pattern optimization of a C-band Phased Array Feed for the Sardinia Radio Telescope. In Proceedings of the 2019 IEEE 2nd Ukraine Conference on Electrical and Computer Engineering (UKRCON), Lviv, Ukraine, 2–6 July 2019; pp. 137–143. [CrossRef]
11. Navarrini, A.; Scalambra, A.L.; Melis, A.; Rusticelli, S.I.; Concu, R.; Ortu, P.; Naldi, G.; Pupillo, G.; Maccaferri, A.N.; Cattani, A.L.; et al. The Warm Receiver Section and the Digital Backend of the PHAROS2 Phased Array Feed. In Proceedings of the 2019 IEEE International Symposium on Phased Array System & Technology (PAST), Waltham, MA, USA, 15–18 October 2019; pp. 1–8. [CrossRef]
12. Schirru, L.; Pisanu, T.; Navarrini, A.; Urru, E.; Gaudiomonte, F.; Ortu, P.; Montisci, G. Advantages of Using a C-band Phased Array Feed as a Receiver in the Sardinia Radio Telescope for Space Debris Monitoring. In Proceedings of the 2019 IEEE 2nd Ukraine Conference on Electrical and Computer Engineering (UKRCON), Lviv, Ukraine, 2–6 July 2019; pp. 133–136. [CrossRef]
13. Valente, G.; Pelorossi, F.; Serra, G.; Urru, E.; Saba, A.; Iacolina, M.; Ghiani, R.; De Vicente, J.; Besso, P.; Buffa, F.; et al. The Optical Design of the Sardinia Deep Space Antenna for Telemetry, Tracking, and Command. *IEEE Access* **2024**, *12*, 141653–141670. [CrossRef]
14. Navarrini, A.; Melis, A.; Comoretto, G.; Pisanu, T.; Nesti, R.; Marongiu, P.; Ortu, P.; Maxia, P.A.; Ladu, A.; Ghobadi, H.; et al. Architecture of C-band Phased Array Feed with RFSoC digital beamformer. In Proceedings of the 2022 3rd URSI Atlantic and Asia Pacific Radio Science Meeting (AT-AP-RASC), Gran Canaria, Spain, 30 May–4 June 2022. [CrossRef]
15. Maxia, P.; Pisanu, T.; Cabras, A.; Pilia, S.; Caocci, R.; Ortu, P.; Melis, A.; Navarrini, A.; Di Ninni, P.; Nesti, R.; et al. Progress in the design of the front-end of the C-Band PAF prototype for the SRT Primary Focus. In Proceedings of the 2024 4th URSI Atlantic Radio Science Meeting (AT-RASC), Meloneras, Spain, 19–24 May 2024. [CrossRef]

16. Pisanu, T.; Maxia, P.; Cabras, A.; Schirru, L.; Ortu, P.; Melis, A.; Navarrini, A.; Belluso, M.; Billotta, S.; Comoretto, G.; et al. Status of a C-band Phased Array Feed with RFSoC digital beamformer. In Proceedings of the 2023 XXXVth General Assembly and Scientific Symposium of the International Union of Radio Science (URSI GASS), Sapporo, Japan, 19–26 August 2023. [CrossRef]
17. Cicchetti, R.; Cicchetti, V.; Faraone, A.; Foged, L.; Testa, O. A Compact High-Gain Wideband Lens Vivaldi Antenna for Wireless Communications and Through-the-Wall Imaging. *IEEE Trans. Antennas Propag.* **2021**, *69*, 3177–3192. [CrossRef]
18. Wang, M.; Crocco, L.; Li, M.; Cavagnaro, M. Slot-Loaded Vivaldi Antenna for Biomedical Microwave Imaging Applications: Influence of Design Parameters on Antenna's Dimensions and Performances. *Sensors* **2024**, *24*, 5368. [CrossRef] [PubMed]
19. Hu, R.; Zhang, F.; Ye, S.; Fang, G. Ultra-Wideband and High-Gain Vivaldi Antenna with Artificial Electromagnetic Materials. *Micromachines* **2023**, *14*, 1329. [CrossRef] [PubMed]
20. Sun, H.; Lee, Y.H.; Luo, W.; Ow, L.F.; Yusof, M.L.M.; Yucel, A.C. Compact Dual-Polarized Vivaldi Antenna with High Gain and High Polarization Purity for GPR Applications. *Sensors* **2021**, *21*, 503. [CrossRef]
21. Ullah, R.; Ullah, S.; Faisal, F.; Ullah, R.; Choi, D.; Ahmad, A.; Kamal, B. High-Gain Vivaldi Antenna with Wide Bandwidth Characteristics for 5G Mobile and Ku-Band Radar Applications. *Electronics* **2021**, *10*, 667. [CrossRef]
22. Saleh, S.; Saeidi, T.; Timmons, N. Simple Compact UWB Vivaldi Antenna Arrays for Breast Cancer Detection. *Telecom* **2024**, *5*, 312–332. [CrossRef]
23. McCulloch, M.A.; D'Cruze, M.; Grainge, K.; Keith, M.; Melhuish, S. A S-Band Cryogenic Phased Array Feed for Radio Astronomy. *RAS Tech. Instrum.* **2023**, *2*, 432–440. [CrossRef]
24. Fan, J.; Yang, J.; Yan, Y.; Zhu, K.; Jiang, P.; Cao, H.; Ma, J.; Li, B.; Pantaleev, M. Design of Octave-Bandwidth Phased Array Feed for Large Radio Telescope. In Proceedings of the 13th European Conference on Antennas and Propagation (EuCAP), Krakow, Poland, 31 March–5 April 2019; ISBN 978-88-907018-8-7.
25. Mailloux, R.J. *Phased Array Antenna Handbook*, 2nd ed.; Artech House: Houston, TX, USA, 2005; ISBN 1-58053-689-1.
26. Rutschlin, M.; Iluz, Z. Phased Array Design with CST STUDIO SUITE. In Proceedings of the 10th European Conference on Antennas and Propagation (EUCAP), Davos, Switzerland, 10–15 April 2016. [CrossRef]
27. Arts, M.; Ivashina, M.; Iupikov, O.; Bakker, L.; Van der Brink, R. Design of a Low-Loss Low-Noise Tapered Slot Phased Array Feed for Reflector Antennas. In Proceedings of the 4th European Conference on Antennas and Propagation (EUCAP), Barcelona, Spain, 12–16 April 2010; ISSN 2164–3342.
28. Kindt, R.W.; Pickles, W.R. Ultrawideband All-Metal Flared-Notch Array Radiator. *IEEE Trans. Antennas Propag.* **2010**, *58*, 3568–3575. [CrossRef]
29. Yan, J.; Gogineni, S.; Camps-Raga, B.; Brozena, J. A Dual-Polarized 2–18 GHz Vivaldi Array for Airborne Radar Measurements of Snow. *IEEE Trans. Antennas Propag.* **2016**, *64*, 781–785. [CrossRef]
30. Shin, J.; Schaubert, D.H. A Parameter Study of Stripline-Fed Vivaldi Notch-Antenna Array. *IEEE Trans. Antennas Propag.* **1999**, *47*, 879–886. [CrossRef]
31. Dhawan, R.; Kaur, G. Vivaldi Antenna Simulation on Defining Parameters, parametric study and results. *Int. J. Circuit Theory Appl.* **2016**, *9*, 5129–5138.
32. Johnson, R.C. *Antenna Engineering Handbook*; Mc Graw-Hill: New York, NY, USA, 1984; ISBN 0-07-032381-X.
33. Milligan, T.A. *Modern Antenna Design*, 2nd ed.; Wiley & Sons: Hoboken, NJ, USA, 2005; ISBN 13 978-0-471-45776-3.
34. Yngvesson, K.S.; Korzeniowski, T.L.; Kim, Y.; Kollberg, E.L.; Johansson, J.F. The Tapered Slot Antenna—A New Integrated Element for Millimeter-Wave Applications. *IEEE Trans. Microw. Theory Tech.* **1989**, *37*, 365–374. [CrossRef]
35. Madhav, P.V.; Prasad, M.S.G. Characterization of Printed Podal Vivaldi Antenna on RT Duroid with Single and Double Cavity. *Int. J. Recent Technol. Eng. IJRTE* **2019**, *7*, 1984–1989. [CrossRef]
36. Yngvesson, K.S.; Shaubert, D.H.; Korzeniowski, T.L.; Kollberg, E.L.; Thungren, T.; Johansson, J.F. Endfire Tapered Slot Antennas on Dielectric Substrates. *IEEE Trans. Antennas Propag.* **1985**, *33*, 1392–1400. [CrossRef]
37. Hayman, D.B. Beamforming and Evaluation of Focal Plane Arrays for Radio Astronomy. Ph.D. Thesis, Macquarie University, Sidney, Australia, 2011.
38. Ivashina, M.V.; Kehn, M.N.M.; Kildal, P. Optimal Number of Elements and Elements Spacing of Wide-Band Focal Plane arrays for a New Generation Radio Telescopes. In Proceedings of the Second European Conference on Antennas and Propagation (EuCAP), Edinburgh, UK, 11–16 November 2007. [CrossRef]
39. Kahkonen, H.; Ala-Laurinaho, J.; Viikari, V. A Modular Dual-Polarized Ka-Band Vivaldi Antenna Array. *IEEE Access* **2022**, *10*, 36363–36372. [CrossRef]
40. Kahkonen, H.; Ala-Laurinaho, J.; Viikari, V. Dual-Polarized Ka-Band Vivaldi Antenna Array. *IEEE Trans. Antennas Propag.* **2020**, *68*, 2675–2683. [CrossRef]
41. Burnett, M.C.; Warnick, K.F.; Jeffs, B.D. ALPACA: The Advanced L-Band Phased Array Camera For Astronomy. In Proceedings of the Phased Array Feed & Advanced Receiver Workshop, Sidney, Australia, 15–17 November 2022.

42. Hesari, S.S.; Locke, L.; Knee, L.; Bornemann, J. Low Cost Phased Array Feed System for Radio Astronomy and Wide-Angle Scanning Applications. In Proceedings of the 2019 IEEE International Symposium on Phased Array System and Technology, Waltham, MA, USA, 15–18 October 2019. [CrossRef]
43. Heyminck, S.; Wieching, G.; Kasemann, C.; Pütz, P.; Barr, E.; Polch, O.; Klein, B.; Leinz, C.; Kraus, A.; Kramer, M.; et al. First Generation Cryo-PAF for Effelsberg. In Proceedings of the Phased Array Feed & Advanced Receiver Workshop, Sidney, Australia, 15–17 November 2022.
44. Wang, J.; Jin, C.; Peng, B.; Zhu, Y. Preliminary Simulation and Manufacture of a 40-element PAF Prototype for FAST. *Res. Astron. Astrophys.* **2023**, *23*, 085009. [CrossRef]
45. Wang, K.; Cao, L.; Ma, J.; Duan, X.F.; Yan, H.; Chen, M.Z.; Ning, Y.W. Development of a Front End Array for Broadband Phased Array Receiver. *Res. Astron. Astrophys.* **2024**, *24*, 045005. [CrossRef]
46. PHAROS: Phased Arrays for Reflector Observing Systems. *System Specifications*, Requirements Specifications, Version 0.7. April 2005.
47. Vishwas, A.; Gull, G.E.; Parshley, S.C.; Cortes-Medellin, G.; Campbell, D.B.; Herter, T.L.; Groppi, C.E.; Burnett, M.C.; Warnick, K.F.; Jeffs, B.D. Assembling the Cryogenic Front-end for the ALPACA Phased Array Feed. In Proceedings of the 2023 IEEE USNC-URSI Radio Science Meeting, Portland, OR, USA, 23–28 July 2023.